Modification of anatase using noble-metals (Au, Pt, Ag): Toward a nanoheterojunction exhibiting simultaneously photocatalytic activity and plasmonic gas sensing

Mohamed Karmaoui [a,*], Luc Lajaunie [b], David Maria Tobaldi [c], Gianluca Leonardi [d], Chahinez Benbayer [e], Raul Arenal [b,f,**], Joāo A. Labrincha [c], Giovanni Neri [d]

[a] School of Chemistry-College of Engineering and Physical Sciences, University of Birmingham Edgbaston, Birmingham B15 2TT, United Kingdom, United Kingdom
[b] Laboratorio de Microscopías Avanzadas, Instituto de Nanociencia de Aragoín, Universidad de Zaragoza, 50018 Zaragoza, Spain
[c] Department of Materials and Ceramic Engineering/CICECO–Aveiro Institute of Materials, University of Aveiro, Campus Universitàrio de Santiago, 3810-193 Aveiro, Portugal
[d] Department of Engineering, University of Messina, Messina 98166, Italy
[e] Department of Industrial Chemistry, Faculty of Chemistry, University of Sciences and Technology of Oran, BP 1505 El M'Naouar, Oran, 31000, Algeria
[f] ARAID Foundation, 50018 Zaragoza, Spain

ARTICLE INFO

ABSTRACT

A new and original method, based on a non-aqueous sol–gel process, has been successfully established to produce quasi-spherical monodispersed TiO_2 nanoparticles (NPs) and also noble metals (NM) @TiO_2 heterostructures (NM = Au, Pt, Ag, 2 wt%), in one-pot and at low temperature. This has been achieved by using titanium oxyacetylacetonate as new single source precursors. This system has been deeply investigated by advanced characterization techniques. By using NMR, we have demonstrated the relatively complex mechanism behind this apparently simple synthesis, mediated by the reaction of the solvent and generated species, with many separate organic and organometallic molecules identified as being involved in the mechanism. The morphology and structure of the NM@TiO_2 heterostructures were investigated by advanced scanning transmission electron microscopy while the chemical state of the noble metal nanoparticles was check by X-ray photoelectron spectroscopy (XPS). Undoped and noble metal (Au, Pt, Ag) decorated quasi/spherical TiO_2 nanoparticles worked also as sensing interfaces, leading to the development of a highly sensitive conductometric NO gas sensor under both dark and UV–vis light irradiation, in the first result of its kind. Furthermore, the photocatalytic activity (PCA) was also evaluated, in the gas–solid phase, by monitoring the degradation of NO_x under solar-light irradiation. Au-modified TiO_2 showed improved photocatalytic efficiencies, compared to unmodified TiO_2.

1. Introduction

With the increasing importance of nanoscience, modern era can be doubtlessly named as the "Nanotechnology Era". The development of advanced materials is shaping the source of technological progress, and involves consistent and flexible synthesis methods.

Multi-functional nanomaterials simultaneously showing different properties, *i.e.* photocatalytic, magnetic, optic and gas sensing properties, have attracted much attention due to their fancy application in many fields [1]. With the aim of design a material exhibiting various coexisting properties, several approaches are usually followed; one of the most en-vogue is to carefully select molecular building blocks, each of which gives a desired chemical or physical property to the final product [2–5]. In this work, we engineered a multifunctional material, taking advantage of the well-known photocatalytic activity of titanium dioxide (TiO_2), and coupling them with the surface plasmon resonance (SPR) characteristics of noble metals nanoparticles (NPs) [6]. When the conducting electrons on

the surface of the metallic NPs are exposed to a specific electromagnetic radiation, they do enter into a collective oscillation/excitation mode (*i.e.* a plasmon), induced by the electric field of the incident light, thus giving rise to the SPR phenomenon [7,8]. The aim here is to design a material− *via* a novel non-aqueous process− possessing at the same time both remarkable photocatalytic and gas sensing properties.

The nature and reactivity of metal oxide precursor are one of the most important parameters for the gel structures. A careful choice of reaction parameters, such as the nature of metal oxide precursor and synthesis temperature, permits to achieve large-scale synthesis of shape-controlled monodisperse titanium nanocrystals (NCs). The selected metal oxide precursor materials used in the preparation of the TiO$_2$ nanoparticles are usually inorganic metal salts or metal organic compounds such as metal (-chlorides, butoxide, ethoxide, isopropoxide, −sulfates) [9–14]. Amongst these, metal isopropoxide is widely used in sol-gel synthesis [15–17]. Our objective is to develop a straightforward route for the preparation of TiO$_2$ NCs without the use all of these precursors in order to produce different nanoparticles in terms of size, size distribution, composition, crystallinity, morphology fortuning their electronic structure. Titanium source such as chlorides, butoxide, ethoxide, isopropoxide, −sulfates have been used to make TiO$_2$ NPs. However, to the best of our knowledge, the use of a metal oxide precursor, such as titanium oxyacetylacetonate Ti(OR), as a way of fabricating small TiO$_2$ NPs has not been reported. Thus, in this paper, we have developed a titanium oxyacetylacetonate non-aqueous sol-gel route for producing TiO$_2$ metal oxide nanoparticles and NM@TiO$_2$ heterostructure where (2 wt%) NM = Au, Pt, Ag. The new solvothermal synthesis through new single metal oxide precursor in 1-hexanol leads to the formation of small crystalline TiO$_2$ NPs and highly dispersible noble metal on TiO$_2$ NPs' surfaces. In this approach the Ti(OR), acting as the starting metal oxide precursor, reacts directly with an aliphatic alcohol to form the TiO$_2$ NCs (see below, Scheme 1); the TiO$_2$ NCs were produced in one pot at low temperature (180 °C), in absence of water, surfactant of any others organic medium.

Microstructure (crystalline domain shape, size and size distribution) of the TiO$_2$ NPs synthesised powders were studied by means of an advanced X-ray method: the whole powder pattern modelling (WPPM) technique, as well as other complementary techniques: nuclear magnetic resonance spectroscopy (NMR), high-resolution (scanning) transmission electron microscopy (HR-(S)TEM), X-ray photoelectron spectroscopy (XPS) and diffuse reflectance spectroscopy (DRS).

For the past decades, it has been recognized that photo-catalysis using TiO$_2$ is one of the most efficient processes for the complete destruction of harmful pollutants in both liquid and gas phase into nontoxic final products [18]. Here, the photocatalytic activity of the prepared samples was assessed in the gas-solid phase, monitoring the degradation of nitrogen oxides (NO$_x$).

TiO$_2$ is also considered one of the most important materials for gas sensor applications due to its interesting physical and chemical properties [19]. However, sensors based on TiO$_2$ materials must operate at a high temperature, typically above 200 °C. On the other hand, many advantages and benefits can be provided by the realization of low power consumption devices if reasonable sensing performance can be obtained at room temperature (RT) [20]. Detection of NO$_x$ is beneficial for human health [21], and environmental monitoring [22] where, in case of exhaust gases from power stations, the main component of air-emitted NO$_x$ mixture is NO (90–95% in total) ranging 0–4000 ppm [23]. In this study, the pure and NM@TiO$_2$ nanostructures were examined for the detection of NO at room temperature, evaluating their sensing characteristics under both dark and UV–vis irradiation by using LED at 400 and 470 nm.

2. Experimental

2.1. Chemicals and materials

Titanium(IV) oxyacetylacetonate TiO[CH$_3$COCH=C(O-)CH$_3$]$_2$ (≥90%), Gold(III) chloride ≥99.99% trace metals basis, platinum(II) acetylacetonate 99.99% trace metals basis, silver acetate 99.99% trace metals basis and anhydrous 1-Hexanol (99%) were used, all from Aldrich.

2.2. Synthesis of TiO$_2$ nanoparticles and (2%) Au, Pt, Ag doped TiO$_2$

The synthesis was carried out in a glove box (O$_2$ and H$_2$O <1 ppm). In a typical procedure, 1 mmol (0.5 g) of Titanium(IV) oxyacetylacetonate TiO[CH$_3$COCH=C(O-)CH$_3$]$_2$ were added to 15 mL of anhydrous 1-Hexanol, the reaction mixture was transferred into a stainless-steel autoclave, and carefully sealed. The autoclave was taken out of the glove-box and heated in a furnace at temperatures at 180 °C for 24 h. In the case of the noble metal doped nanoparticles, 2 wt% Titanium(IV) oxyacetylacetonate was replaced by gold chloride, platinum acetylacetonate and silver acetate. The resulting milky suspensions were centrifuged, and the precipitates were thoroughly washed with ethanol and dichloromethane, and dried in air at 60 °C.
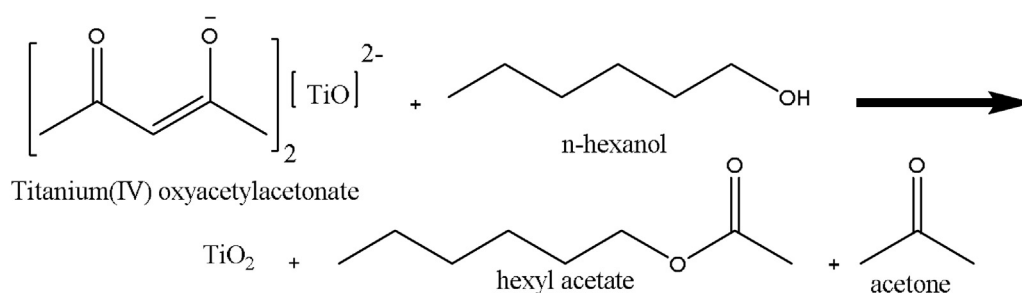
2.3. Sample characterization

X-ray powder diffraction (XRPD) measurements for the crystalline domain size evaluation were performed at room temperature on the dried nanopowders using a PAN alytical X'Pert Pro (NL) θ/θ diffractometer equipped with a fast RTMS detector (PIXcel 1D, PANalytical), using CuK$_\alpha$ radiation in the 2θ range of 20–125° with a virtual step scan of 0.02°, and a virtual integration time of 500 s per step. Microstructural analysis (*i.e.* crystalline domain shape, size and size distribution) of the specimens was solved by means of the whole powder pattern modelling (WPPM) [24], as implemented in the PM2 K software [25]. The instrumental contribution was also obtained, modelling the profile of 14*hkl* reflections from the NIST SRM 660b standard (LaB$_6$), according to the Caglioti et al. relationship [26]. Then, the following parameters were refined: background (6th-order Chebyshev polynomial function), peak intensities, specimen displacement, lattice parameters, mean and variance of the size distributions−crystalline domains were approximated to be spherical, and their diameter distributed according to a lognormal curve.
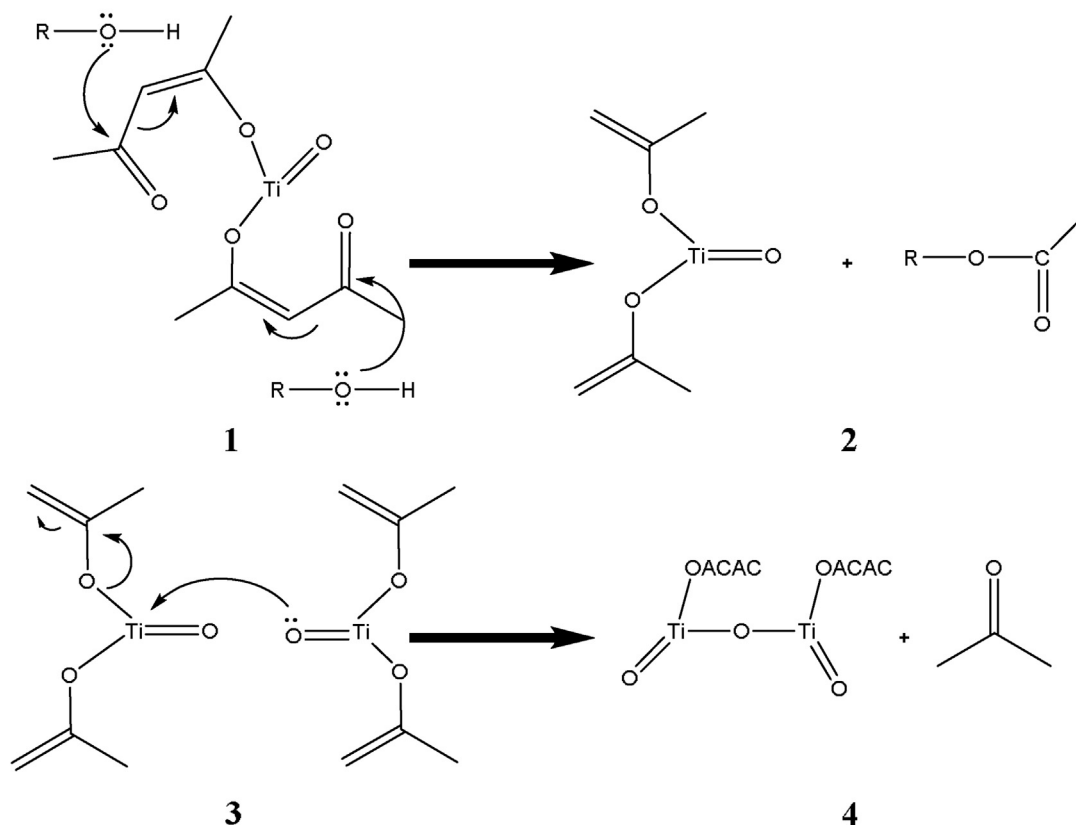
High-resolution scanning transmission electron microscopy (HR-STEM) experiments have been performed using an FEI Titan Low-Base microscope operated at 300 kV and equipped with an energy-dispersive X-ray (EDS) detector, a CESCOR Cs probe corrector, an ultra-bright X-FEG electron source and a monochromator. HR-STEM imaging was performed by using high-angle annular dark field (HAADF) detector and an ADF detector. The inner and outer angles for most of the micrographs recorded with the HAADF and ADF detector were 48 and 200 mrad, and 22 and 12 mrad, respectively.

The X-ray photoelectron spectroscopy (XPS) analyses were carried out using Kratos Axis Ultra and Supra spectrometers. The photoelectron spectra were excited by a soft X-ray Al K$_\alpha$ (1486.6 eV) anode at a power of 150 W (10 mA, 15 kV) and 225 W (15 mA, 15 kV) for the Kratos Ultra and Supra spectrometers, respectively. Calibration of the spectra was done by setting the position of the C1 s peak coming from carbon-based contaminants at 284.9 eV.

Scheme 1. Proposed reaction mechanism occurring during the non-aqueous synthesis of TiO_2 oxide NPs in 1-hexanol.

2.4. Photocatalytic activity

The photocatalytic activity of the prepared specimens, was assessed on a reactor previously described in the literature [15].This was made of a stainless steel cylinder (35 L, internal volume), and operated in continuous conditions. This reactor was used to monitor the NO_x abatement (where $NO_x = NO + NO_2$). Samples were prepared in form of thin layer of powder, with a constant mass (∼0.0030 gr), and consequently approximately constant thickness, in a 6-cm diameter Petri dish. A solar lamp (Osram Ultra Vitalux), placed 85 cm from the surface of the photocatalyst, was used. The radiant flux (irradiance) reaching the surface of the samples was estimated, by means of a radiometer, to be ∼ 3.6 W m^{-2} in the UVA range, and 25 W m^{-2} in the visible-light range. PCA tests were performed at $22 \pm 1\,°C$ (temperature inside the reactor) with a rel-ative humidity of 35% − these parameters were controlled through a thermocouple placed inside the chamber, and a humidity sensor placed in the inlet pipe, and they were constrained to remain stable throughout the tests. The outlet concentration of the pollutant gas was measured using a chemiluminescence analyser (AC–30 M, Environment SA, FR). After having placed the photocatalyst inside the reactor, and covered the glass window, the inlet gas mixture (prepared using cylinders with synthetic air and NO_x gas) was allowed to flow until it stabilised at a concentration of 0.2 ppm. Two mass flow controllers were used to prepare a mixture of air with this concentration of NO_x, and with a flow rate of 1 L min^{-1}. When the desired concentration of 0.2 ppm was reached inside the reactor, the window glass was uncovered, the lamp turned on, and the photocatalytic reaction was supposed to start – total irradiation time was set at 55 min. The photocatalytic efficiency was evaluated

as the ratio of the removed concentration of NO_x. The conversion rate (%) of the initial NO_x concentration was calculated as:

$$NO_x conversion\% = \frac{(NO_x)_0 - (NO_x)_S}{(NO_x)_0} \times 100$$

where $(NO_x)_0$ and $(NO_x)_S$ are, respectively, the initial NO_x and the NO_x concentration after a certain irradiation time [27].

2.5. NO sensing

NO sensing tests were carried out on conductometric platforms fabricated using alumina substrates (3×6 mm) supplied with inter-digitated Pt electrodes and heating elements on the back side. Printable paste of sensitive material was obtained mixing TiO_2 based samples with water, then the paste has been screen printed onto the interdigitated electrodes to obtain a thick film ($\sim 10\,\mu m$) with a sensitive geometrical area of 3×3 mm. Thanks to the high porosity of the alumina, no binder was necessary to enhance the adhesion of the sensing layer on the alumina substrate.

All measurements were performed at room temperature in dynamic conditions under a dry synthetic air total stream of 100 sccm, collecting the sensors resistance data in the four points mode by means of an Agilent 34970A multimeter. The sensing tests under UV irradiation were performed in a test chamber (about 10 mL volume) equipped with LED lamps. The gas response is defined as the ratio $S = R_0/R$, where R_0 represents the electrical resistance of the sensor in dry air and R its electrical resistance at different NO concentration.

3. Result and discussion

3.1. NMR, XRD, STEM-HAADF, XPS and UV–vis

We report hereafter the first versatile chemical synthesis of monodisperse titanium metal oxide nanoparticles of controlled size and size distribution as well as that of hybrid dumbbell-like (2 wt%) Au, Pt, Ag: TiO_2. The modulation of their photocatalytic and gas sensing properties are also investigated. The main goal of these works was to assess the possibility to obtain pure TiO_2 NPs without any impurities by employing the greatest useful route via the non-aqueous sol-gel route, as well as improving several of the properties of this system. Based on our previous research interests, TiO_2 metal oxide nanoparticles and NM@TiO_2 heterostructure where (2 wt%) NM = Au, Pt, Ag.

To better understand the possible mechanism formation of the TiO_2 NPs, we have carefully examined the reaction mixture after synthesis; the product was filtered to remove the TiO_2 precipitate. Nuclear magnetic resonance (NMR) spectroscopy (^{1}H and ^{13}C) spectroscopy is a powerful method to characterize the reaction mixture after synthesis, thus, we identified all different organic species in aqueous solution. The ^{13}C NMR spectra collected for the reaction mixture is shown in Fig. 1 (^{1}H NMR spectrum, Supp. Info); and the spectrum showed many different signals corresponding to 1-hexanol and derivative. The analysis of the purified TiO_2 NPs reveals that the majority of the 1-hexanol has been converted to hexanoate and the presence of ketone and hexyl acetate have also been observed in excess of 1-hexanol, (See Table 1, Supp. Info).

The mechanism of formation is based on two possible consecutive steps. In the first step, oxygen coordinates with the carbon of oxyacetylacetonate of titanium metal oxide precursor (1), resulting in a mixed titanium complex with the loss of hexyl acetate (2). The later was proven in ^{13}C NMR. In the second step, the mixed titanium complex (3), which itself reacts with another mixed titanium complex resulting in condensation. This could precipitate, forming TiO_2 metal oxide nanoparticles with ketone (4) side products (Scheme 1). Therefore, the condensation reaction between titanium

oxyacetylacetonate and 1-hexanol with ketone elimination affords a smart method for the formation of TiO_2 metal oxide nanoparticles.

Microstructure of as-prepared TiO_2 NPs and NM@TiO_2 heterostructure were characterized through X-ray diffraction (XRD) and WPPM (Fig. 2). TiO_2 and noble-metal modified TiO_2 NPs, consist all of anatase TiO_2 polymorph. Being anatase the thermodynamically stable phase at the nanoscale [28,29], its presence has to be quite expected. WPPM results are shown in Fig. 2 and Table 1. The crystalline domain size, of unmodified anatase is 5.0 nm in diameter (detected crystalline domain size in the range of around 2–12 nm, mode of the size distribution equal to 4.0 nm). In general, noble metals modification virtually did not alter the anatase crystal size [29], nor its unit cell volume, as it is seen in Fig. 2, and Table 1. From the negligible differences in unit cell volume (Table 1), we can infer that noble-metals did not enter the anatase lattice, however the very slight decrease in the tetragonality (the a/c ratio) of anatase in Ag-and Au-TiO_2, might suggest the occurrence of some local distortion. Furthermore, gold and platinum modifications give anatase a slightly smaller average domain diameter, 4.5 nm versus 5.0 nm of unmodified titania.

The morphology and structure of the noble metals@TiO_2 NPs were also investigated by STEM high-angle annular dark field (HAADF) imaging. Fig. 3a–b shows the STEM-HAADF micrographs of the Pt@TiO_2 system. Two distinct kinds of particles with distinct distribution, contrast, size and shape can be clearly seen. First of all, both kinds of the NPs present a good crystallinity which is clearly seen on the HR-STEM micrographs and on the corresponding fast Fourier transform (FFT) diffractograms (Fig. 3c for the brightest NPs and Fig. 4 for the darkest NPs). Most of the NPs present a darkest contrast, a size between 4 and 10 nm and a square or rectangular shape (Fig. 4). A darkest contrast in STEM-HAADF highlights a lowest mass density and/or a lowest thickness. These NPs should thus be ascribed to the TiO_2 NPs, which have a lower mass density than those of Pt. It is confirmed by analyzing the FFT image (Fig. 4), which corresponds to the TiO_2 anatase crystal structure and are thus in good agreement with the XRD analyses. Finally, the less abundant NPs are well dispersed on the TiO_2 NPs's surface, isolated and present a diameter between 2 and 3 nm (although few of them can attain 10 nm) with a spherical shape (Fig. 3c). These NPs present a brightest contrast than the other one and should thus correspond to the Pt NPs. To confirm this, energy-dispersive X-ray spectroscopy (EDS) [30–32] analyses were recorded on the two kind of NPs (Fig. 3d–e). While the Ti lines can be seen over the whole sample because of the juxtaposition of the two different kinds of NPs, the Pt lines can be ascribed only to the NPs with a brighter contrast. The STEM-HAADF and EDS analyses confirm thus the synthesis of a Pt@TiO_2 heterostructure, the Pt NPs being well dispersed on the TiO_2 matrix, crystalline and with a size between 2 and 3 nm. The exact same statements can be made for the Ag@TiO_2 system (Fig. S3) although the size of the Ag NPs is slightly smaller (between 1 and 2 nm). The situation is slightly different for the Au@TiO_2 system. The Au NPs are less abundant than their Ag counterparts (Fig. 5a) and their size is between 10 and 20 nm (even few of them can attain 50 nm). However, as the Pt and Ag NPs, they present a good crystallinity (Fig. 5b) and a spherical shape.

To confirm these results XPS and Auger analyses were performed on the NM@TiO_2 systems. Fig. 6a shows the XPS Au 4f spectrum of the Au@TiO_2 NPs. The binding energy of the Au $4f_{7/2}$ is at 83.3 eV and the splitting between the $4f_{7/2}$ and $4f_{5/2}$ lines is equal to 3.7 eV. The binding energy of the Au $4f_{7/2}$ line is slightly lower than expected for bulk Au^0 (between 83.8 and 84.0 eV) [33–35]. Such shift to lower energy is commonly observed for metallic nanoparticles and is attributed to geometry and/or confinement effects [36,37]. On the contrary, a shift to higher energy of the Au $4f_{7/2}$ line would indicate an oxidation of the Au NPs [35]. Overall, the XPS analyses confirm thus Au^0 valence state of the Au nanopar-
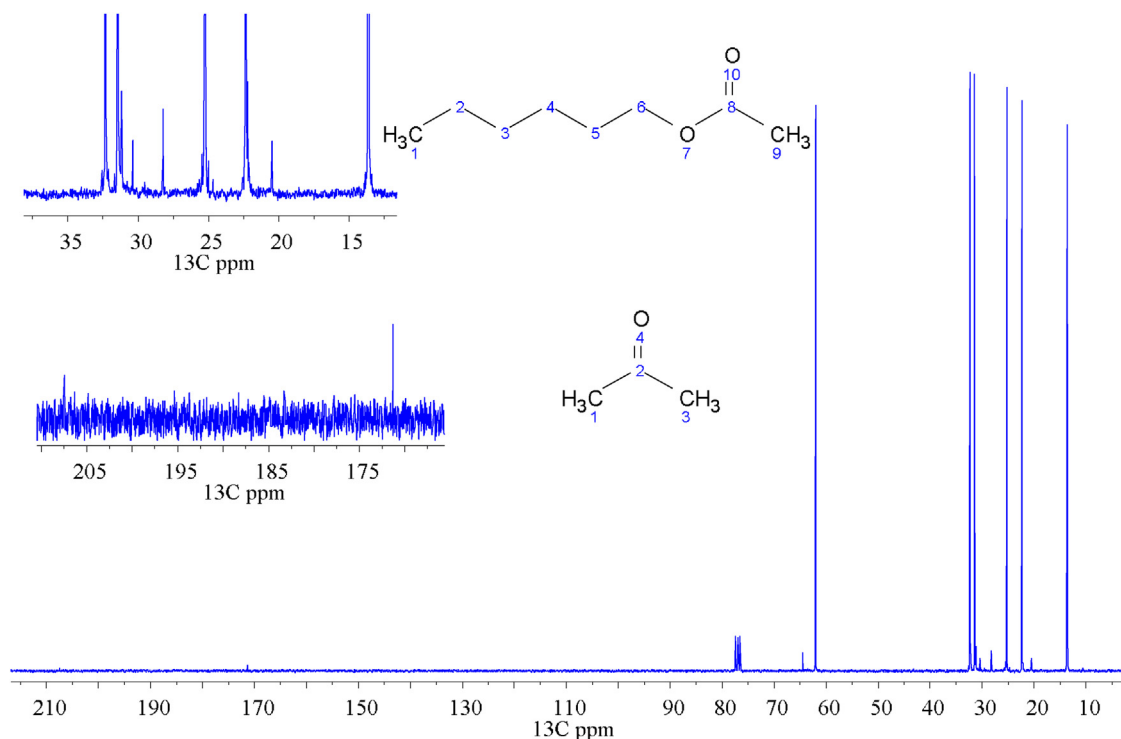
Fig. 1. ^{13}C NMR spectrum of the filtered reaction solution measured in CDCl$_3$ of the TiO$_2$ oxide nanoparticles.
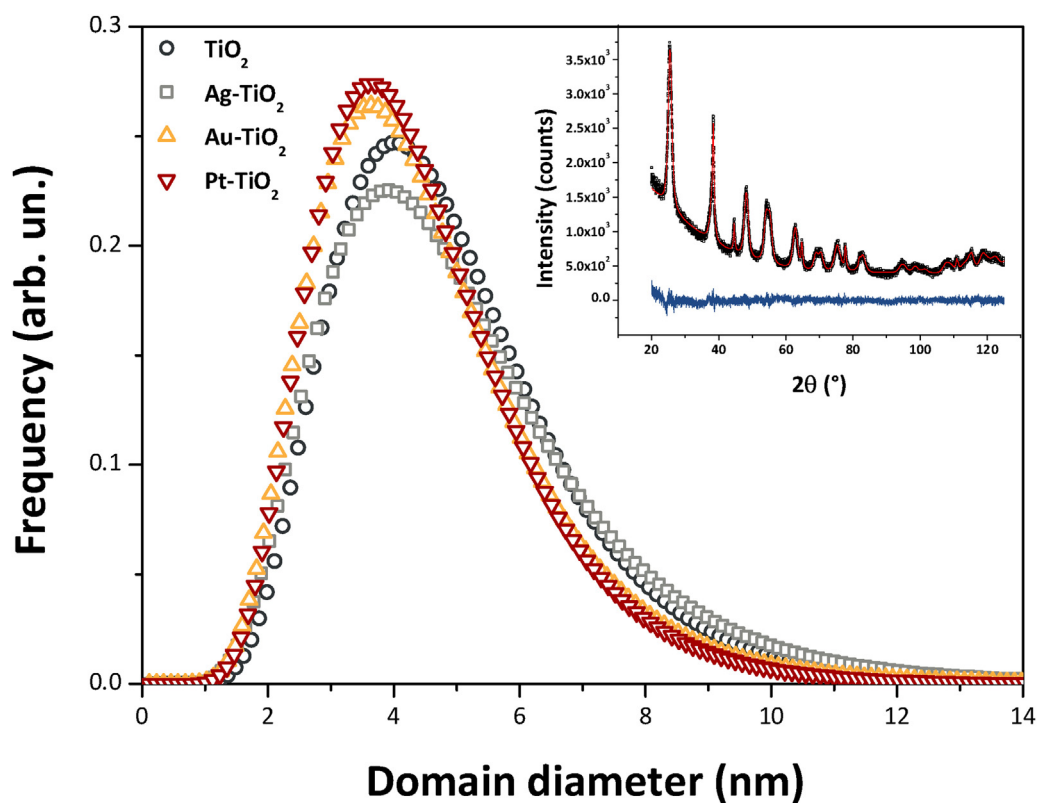

Fig. 2. Size distribution, as obtained from the WPPM modelling of synthesized samples. In the inset is reported the output of the Au-TiO$_2$ WPPM modelling (the black open squares represent the observed data, the red continuous line is the calculated data, the blue continuous line at the bottom is the residual curve). (For interpretation of the references to colour in this figure legend, the reader is referred to the web version of this article.)

ticles. Fig. 6b shows the XPS Ti 4f spectrum of the Au@TiO$_2$ system. The presence of the Ti 3s satellite peak (highlighted by a purple arrow in Fig. 6b) makes difficult a proper interpretation of the raw spectrum. To extract more quantitative information, a modelling of the spectrum was done by constraining the ratio between the integrated areas of the 4$f_{5/2}$ and 4$f_{7/2}$ lines to ¾ in order to take

Table 1
WPPM agreement factors, unit cell parameters, mean and mode of the size distributions.

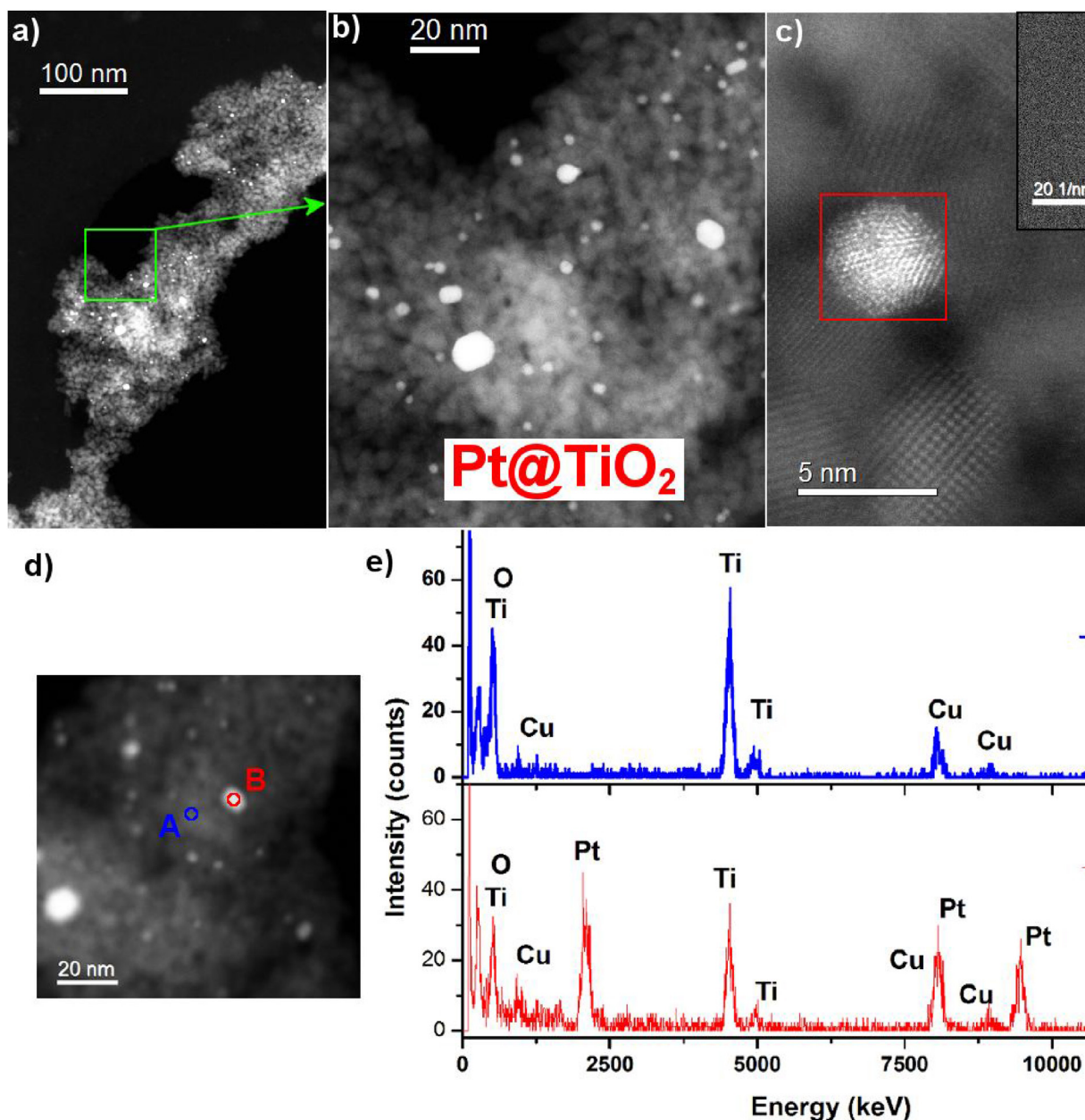| Sample	Agreement factors			Anatase unit cell parameters			Mean crystalline domain size (nm)	Mode of the size distribution (nm)
	R_{wp} (%)	R_{exp} (%)	χ^2	$a = b$ (nm)	c (nm)	V (nm^3)	Anatase	Anatase
TiO$_2$	4.29	2.97	1.44	0.3792(1)	0.9499(1)	0.1366(1)	5.0(1)	4.0(1)
Ag-TiO$_2$	6.14	3.38	1.82	0.3790(1)	0.9508(1)	0.1366(1)	5.1(1)	3.9(1)
Au-TiO$_2$	4.74	3.59	1.32	0.3787(1)	0.9510(1)	0.1364(1)	4.5(1)	3.6(1)
Pt-TiO$_2$	4.72	3.10	1.52	0.3787(1)	0.9487(1)	0.1363(1)	4.5(1)	3.6(1)

Fig. 3. a) Low-magnification and b) medium-magnification STEM-HAADF micrographs of the Pt@TiO$_2$ heterostructure. The green square in *a* highlights the area in which *b* was taken. c) HR-STEM HAADF micrograph of the Pt@TiO$_2$ NPs. The red square highlights the area used to determine the FFT depicted in the inset. d–e) EDS spectra (*right*) acquired on the NPs with the darker and brighter contrasts (labelled *A* and *B* respectively) displayed in the STEM micrograph (*left, (d)*). (For interpretation of the references to colour in this figure legend, the reader is referred to the web version of this article.)

into account the degeneracy of the 4*f* states into $4f_{7/2}$ and $4f_{7/2}$ levels. The binding energy of the Pt $4f_{7/2}$ is at 83.3 eV and the splitting between the $4f_{7/2}$ and $4f_{5/2}$ lines is equal to 3.7 eV. It is in good agreement with Pt^0 valence state even if, once again, the binding energy is slightly lower than the one expected for bulk Pt metal (between

70.8 and 71.7 eV) [38]. The XPS Ag 3*d* spectrum in shown in Fig. 6c. Because of the low signal/noise ratio, directly related to the small NPs size as evidenced by HR-STEM, it is difficult to discard the presence of minor contributions. In addition, the identification of the Ag chemical states based solely on the binding energy of the Ag 3*d*
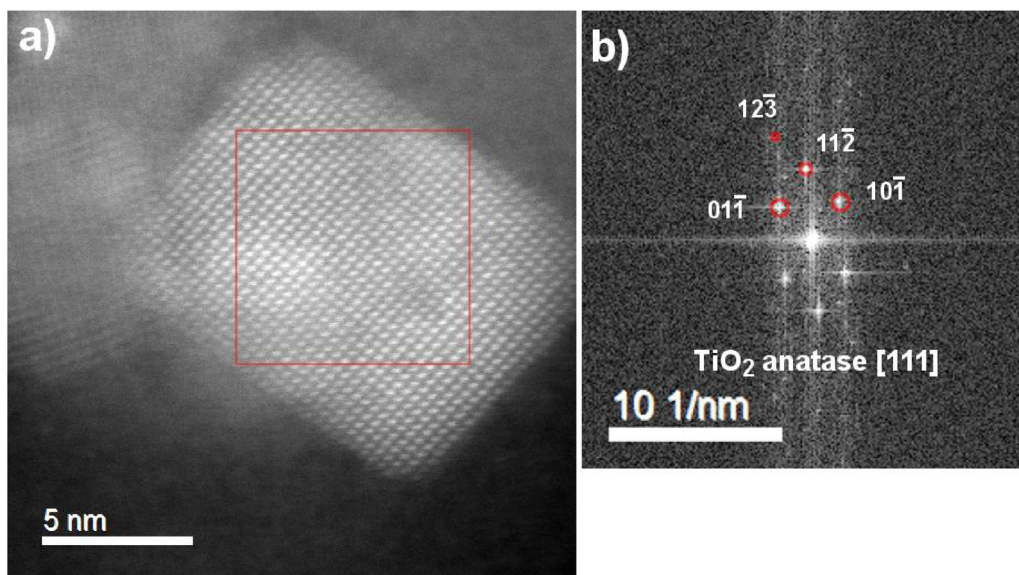
Fig. 4. a) HR-STEM ADF micrographs of one of the more abundant NPs which present a darker contrast. The red square highlights the area used to perform the b) FFT image which has been indexed and corresponds to the TiO_2 anatase crystal structure seen in the [111] zone axis. (For interpretation of the references to colour in this figure legend, the reader is referred to the web version of this article.)

states is challenging because of the small energy shift between Ag^0 and the Ag^+ cation in silver oxide (0.4 eV at maximum) [39]. On the other hand, examination of Auger spectra is useful to identify Ag chemical states [40,41]. The modified Auger α parameter (summation of the kinetic energy of the Auger transition and the binding energy of the core level) is equal to 726.1 and thus corresponds to the Ag^0 valence state [41]. However, the shape of the Auger spectrum as well as the large widths of the Ag 3d lines (full width at the half maximum) (FWHM ∼ 1.8 eV) might indicate the presence of minority species, such as silver oxide. Finally, the atomic concentrations for the Pt and Ag elements are equal to 0.3% and 1% for Au. This confirms the good distribution of the NM NPs over the TiO_2 matrix.

Raman spectroscopy serves as a powerful tool to investigate NPs based on NM@TiO_2 heterostructure. A typical set of Raman spectra is shown in Fig. 7. Indeed, the Raman peaks at 148, 199, 395, 515, 639 cm^{-1} correspond to $E_g(1)$, $E_g(2)$, $B_{1g}(1)$, $A_{1g} + B_{1g}(2)$, and $E_g(3)$ vibration modes of anatase, respectively, thus confirming XRD findings. A very weak and broad shoulder band near 190–195 cm^{-1} is also visible in this spectrum. This indicates the presence of small impurities of Au (Pt, Ag) noble metal nanoparticles in the heterostructure materials [42,43]. The observed Raman bands of (2 wt%) Au, Pt, Ag: TiO_2 NPs match well with the reported literature values and can be assigned accordingly.
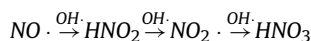
Optical spectroscopy results are shown in Fig. 8. Unmodified and noble-metal modified TiO_2 NPs show an absorption band at around <350 nm, that is assigned to the $Ti^{4+}-O^{2-}$ metal-ligand charge transfer (MLCT) [44]. On the other hand, the absorption edge at ∼380 nm is due to the band-gap transition in the anatase; as a matter of fact, the optical band gap (E_g) of the material was found to be at 378 nm (3.28 eV), fully consistent with anatase's expected E_g [45]. All noble-metals modified TiO_2, beside this band, also display their respective absorption due to the SPR, their position centered at 469, 571, and 483 nm for Ag-, Au-, and Pt-TiO_2 systems, respectively. However, at this regard, it has to be underlined that the position of SPR band strongly depends directly upon different factors, such as: the noble-metal NPs shape [46,47] and size [7] (even within a given medium [48], and also upon the distance between neighboring noble-metal NPs.)[49–51]. This means that, for instance, as the particle size decreases, the center of the

plasmon band blue-shifts, and *vice-versa*. Moreover, NM NPs are here embedded in a TiO_2 matrix that, possessing a high relative permittivity [52], will result in light being absorbed at longer wavelengths, as it is actually the case of our NM NPs anatase systems. It is also known that small noble-metal NPs give a wide SPR band [53], having a certain size distribution, and this is the case of our noble-metals modified TiO_2 (*cf* Fig. 8).

4. Functional properties

4.1. Photocatalytic activity

Photocatalytic activity (PCA) of NO_x abatement results are reported in Fig. 9. As it is can be seen, all the samples are photocatalytically active materials. According to literature reports, it is now well-known that NO_x photocatalytic conversion progresses in individual one-electron transfer step, through the production of intermediate species − *i.e.* nitrous acid (HNO_2) and nitrogen dioxide (NO_2). The final product of the degradation is nitric acid (HNO_3) [54]:

$$NO \cdot \overset{OH\cdot}{\rightarrow} HNO_2 \overset{OH\cdot}{\rightarrow} NO_2 \cdot \overset{OH\cdot}{\rightarrow} HNO_3$$

With the experimental conditions used (a lamp simulating the solar spectrum, and nitrous oxide abatement), Au-TiO_2 is the most active sample, followed by: Ag-TiO_2 ≈ TiO_2 > Pt-TiO_2. It is well-established that noble-metals NPs decorated on the surface of TiO_2 have a positive influence on TiO_2 PCA [55]. This is attributed to the aptitude of plasmonic noble metals to concentrate and scatter visible light, thus helping in harvesting solar energy. In general, when a semiconductor-noble metal heterojunction system is irradiated with UV-light, the electrons at the valence band of the semiconductor are promoted to the conduction band, and then they are transferred to the Fermi level of the noble-metal, thus favoring the separation of e^-/h^+ photo-generated pair [56,57]. On the other hand, when this system is exposed to visible light, charge carriers (*i.e.* "hot electrons") [58] are formed in the noble metals, because of the absorption of visible light; these charge carriers are then directly injected from excited plasmonic-metal nanostructure to the semiconductor material [59,60]. These phenomena are able to explain the greater PCA of the noble-metal/TiO_2 systems, compared
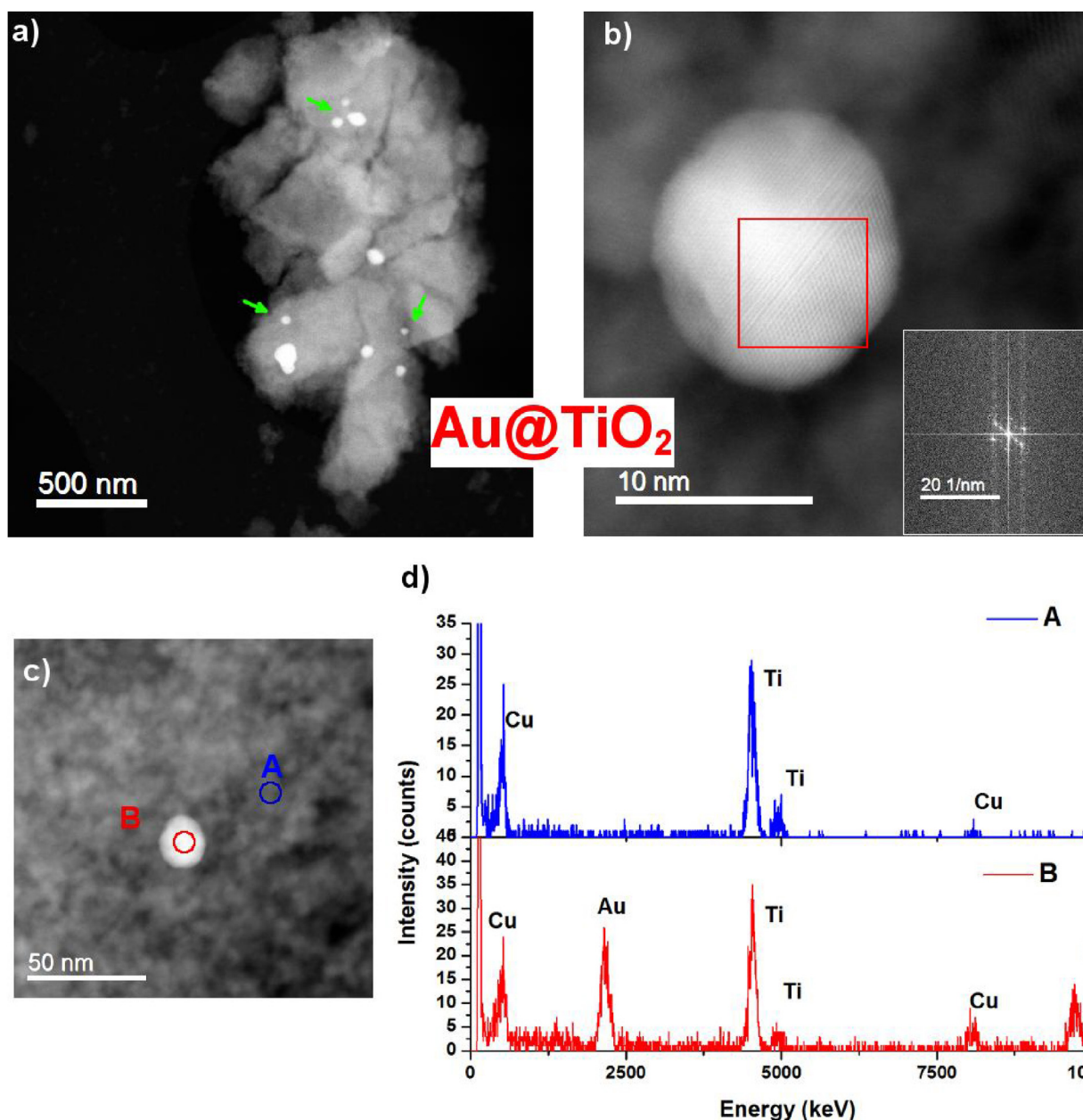
Fig. 5. a) Low-magnification STEM-HAADF and b) HR-STEM-HAADF micrographs of the Au@TiO$_2$ NPs. The red square highlights the area used to determine the FFT seen in the inset. c–d) EDS spectra taken on the NPs with the darker and brighter contrast (labelled *A* and *B,* respectively). (For interpretation of the references to colour in this figure legend, the reader is referred to the web version of this article.)

to the bare TiO$_2$, as we used a lamp simulating the solar spectrum (*i.e.* a lamp with both UV and visible component).

In the case of Au-TiO$_2$, *i.e.* the best performing photocatalyst amongst this series, its higher PCA can be explained taking into consideration the electrochemical potentials of the band edges of anatase and Au NPs, with respect to the absolute vacuum scale (AVS), as depicted in Scheme 2:

When the Au-TiO$_2$ system is irradiated by the solar lamp, is able to absorb visible-light because of the SPR of Au NPs. By absorbing visible-light, electrons from Au are generated, and transferred to the conduction band of anatase, to leave hole in the Au NPs. Those electrons are thus able to reduce the oxygen adsorbed on the surface of TiO$_2$, to generate superoxide ($O_2^{\bullet-}$), that have been recognized to be the main active reactive oxygen species (ROS), responsible for the reduction of NO [63].

On the contrary, the coexistence of Ag^0 and Ag oxides and the lowest concentration of Ag and Pt, as pointed out by XPS study, can explain the reduced PCA of Ag@TiO$_2$ and Pt@TiO$_2$ heterostructures when compared to Au@TiO$_2$ [64].

The lower PCA of Pt-TiO$_2$ can be justified by the radiation used in the test. This is indeed consistent with results obtained in a very recent investigation by Hernández Rodríguez and co-authors [65]. They actually found that with UVA-light, Pt modified titania did not show any significant improvement in NO photocatalytic oxidation compared with unmodified TiO$_2$; this was attributed to a higher recombination of the photo-generated electron-hole pair when using a UVA-lamp, thus becoming the dominant process [64]. On the contrary, with the same UVA-light, Au-modified TiO$_2$ showed itself improved photocatalytic efficiencies, if compared to unmodified TiO$_2$. Thus, being the light used in this work a solar light − *i.e.* with both UVA and visible component, and being the UVA-
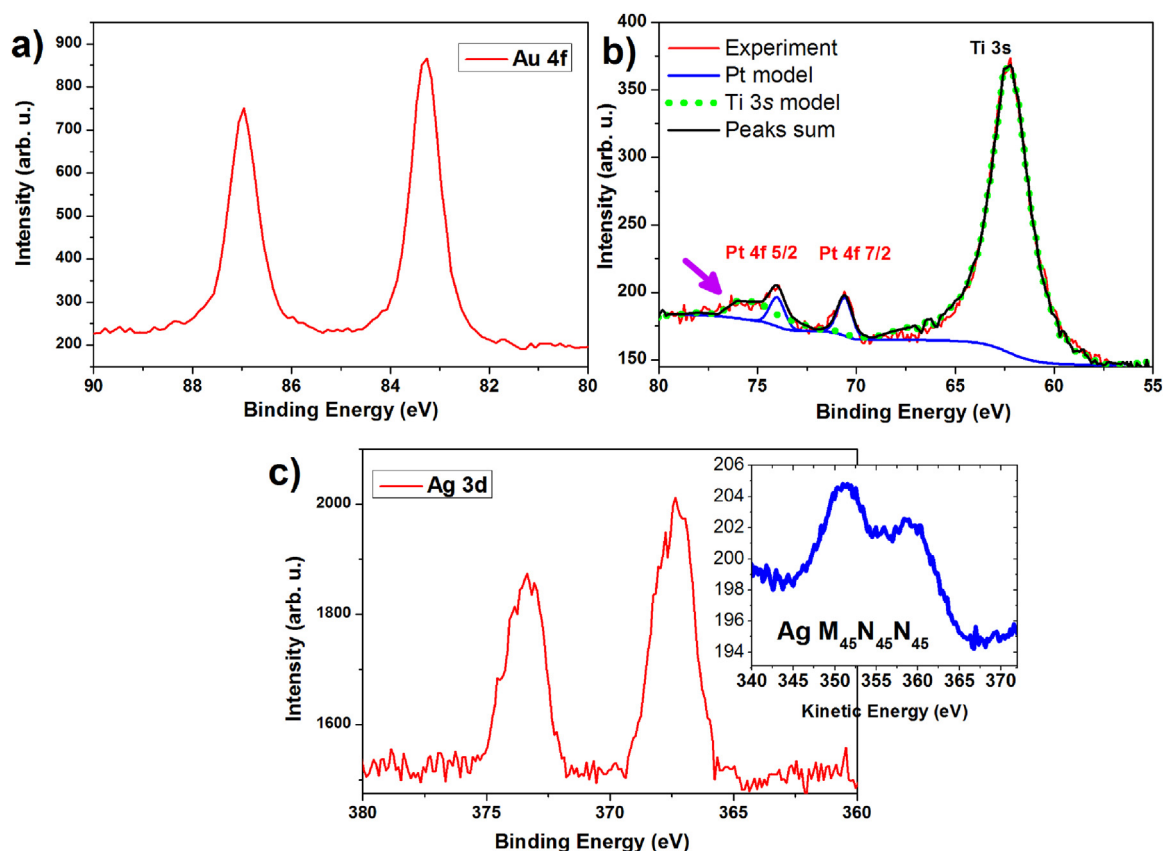
Fig. 6. a) XPS Au 4*f* spectrum of the Au@TiO$_2$ system. b) XPS Ti 4*f* spectrum of the Ti@TiO$_2$ system. The purple arrow highlights the position of the Ti 3*s* satellite peak. c) XPS Au 3*d* spectrum of the Ag@TiO$_2$ system. The inset shows the corresponding M$_{4,5}$N$_{4,5}$N$_{4,5}$Auger electron spectrum.
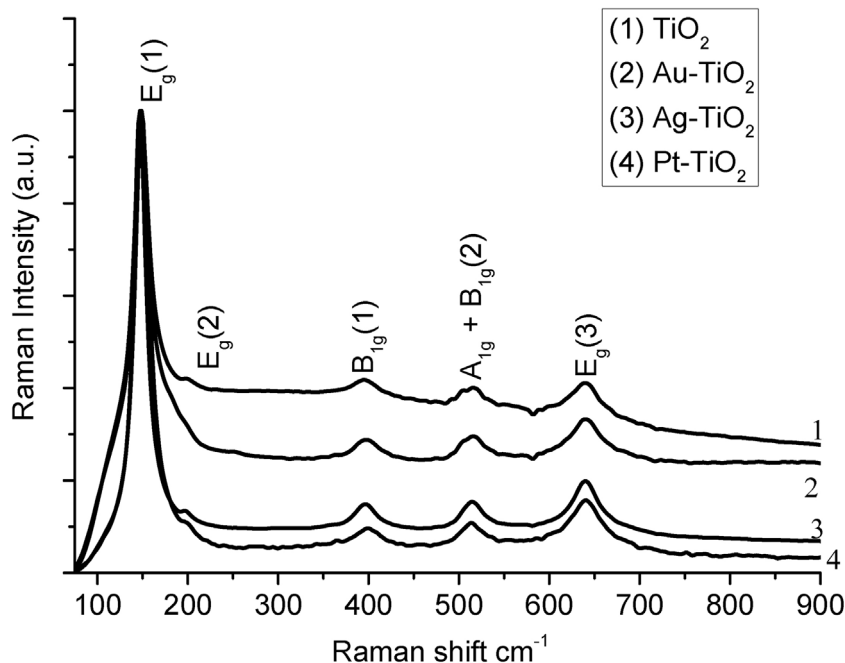

Fig. 7. Raman spectra of undoped and 2 wt% noble metal doped TiO$_2$ NCs depicting different phonon modes of pure anatase TiO$_2$ (**1**), Au-TiO$_2$ (**2**) Ag-TiO$_2$ (3), and Pt-TiO$_2$ (4) using the solvothermal synthesis at 180 °C during 24 h.

component not negligible − we infer that the UVA-component of the lamp is of hindrance to the PCA of Pt-TiO$_2$ specimens.

4.2. NO sensing

Inspired by the good photocatalytic properties of synthesized materials, we tried to develop a conductometric sensor for NO mon-
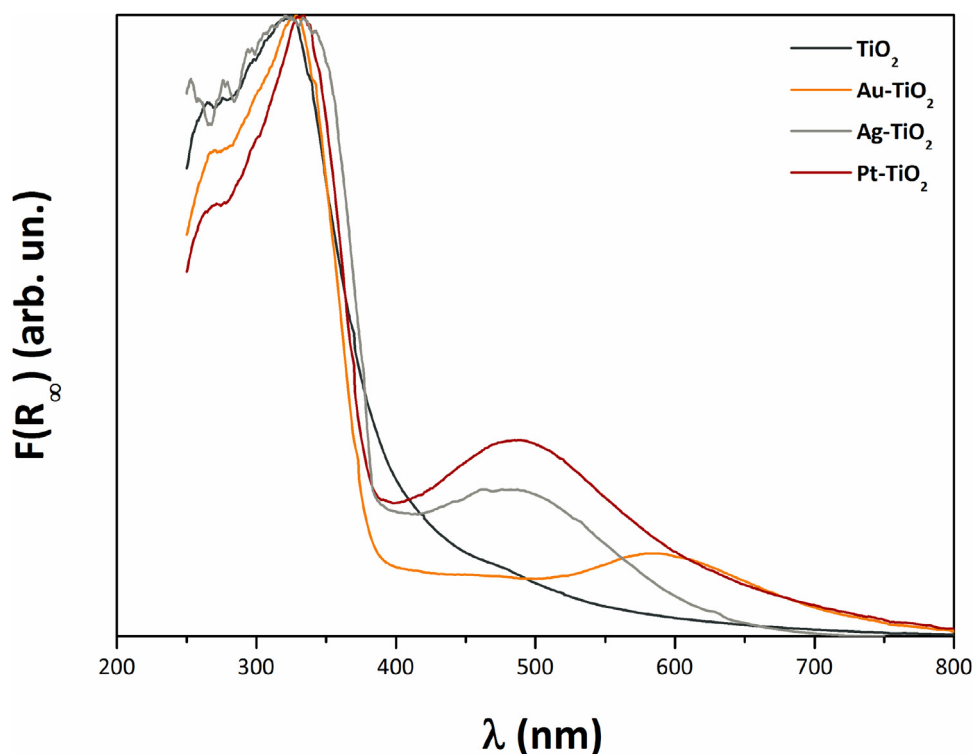
Fig. 8. DRS spectra of different prepared specimens (Ag-, Au-, and Pt-TiO$_2$ NPs, as well as unmodified TiO$_2$ NPs).
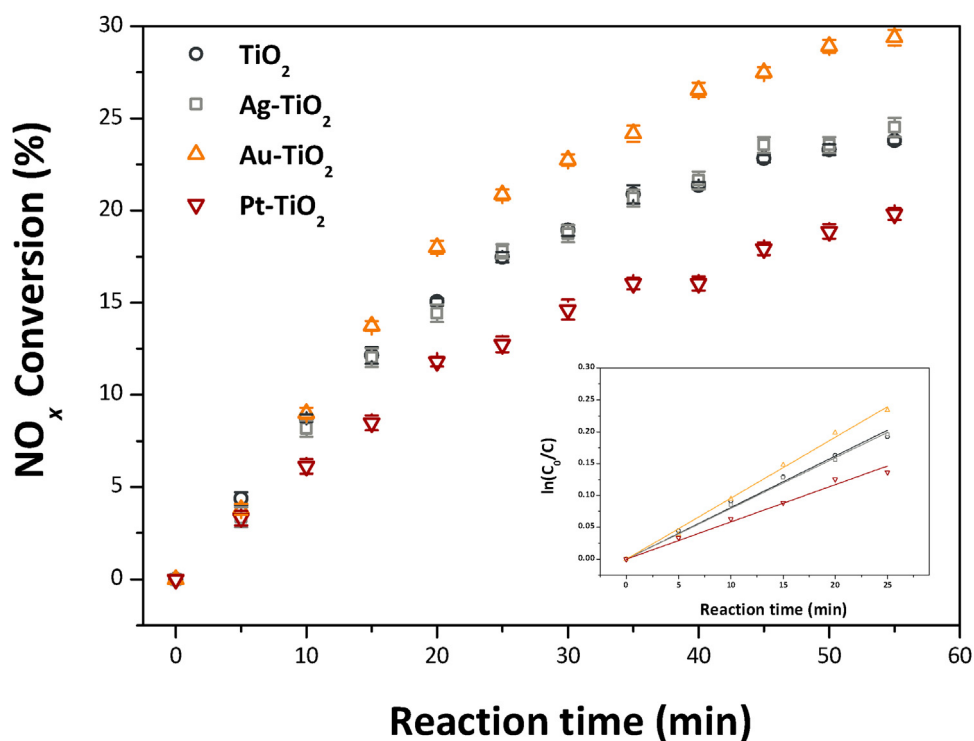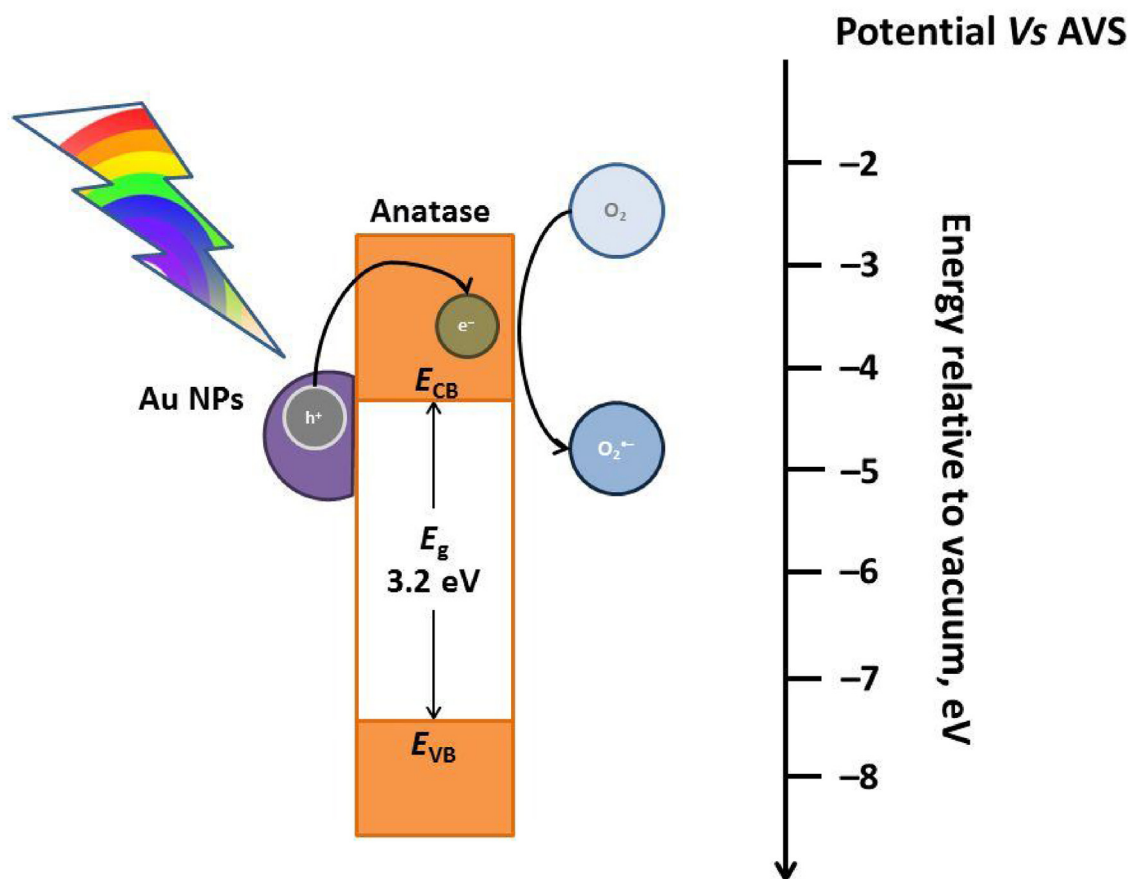

Fig. 9. Photocatalytic activity (NO$_x$ abatement) of prepared specimens. In the inset is reported the ln(C$_0$/C) versus reaction time for the different samples.

itoring in air. A search in the past literature revealed that there is limited work about conductometric sensors for NO detection over TiO$_2$-based sensors [66,67]. Furthermore, no work investigating the effect of promoters on the sensor performances appeared so far. First, NO gas sensing properties of the synthesized TiO$_2$ nanostructures were investigated upon exposure to 100 ppm NO gas diluted in humid air (RH = 50%) at RT under dark conditions. On all sensors, the baseline resistance in air decreases after NO pulses, as shown by the dynamic response of the Au-TiO$_2$ gas sensor reported in Fig. 10.

This behavior suggests that, under the conditions adopted, theTiO$_2$-based semiconductors show a *p*-type characteristics, because upon exposure to electron accepting gases such as NO,

Potential *Vs* AVS

Scheme 2. Proposed mechanism for the prolonged lifetime of the photo-generated pair (e−/h+) in an anatase TiO$_2$ decorated with Au NPs. Electrochemical potentials of the band edges of anatase and Au NPs, with respect to the absolute vacuum scale (AVS), are from the literature [61,62].
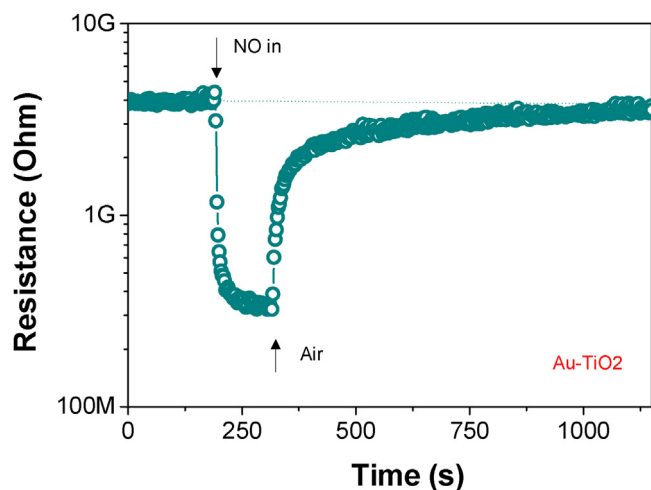

Fig. 10. Resistance variation of the Au-TiO$_2$ sensor to 100 ppm of NO in air at room temperature under dark conditions.

Fig. 11. Response of Au-TiO$_2$ to repeated pulses of NO (100 ppm).

the electron charge transfer resulted in an enrichment of the hole carriers and consequently in a decrease of the resistance.

Repeatability (cyclic on-off) sensing tests have been carried. Results demonstrated the baseline stability and reversible and repeatable response of the sensor tested. As an example, we have added a figure in the main amended manuscript, showing the response of Au-TiO$_2$ to repeated pulses of NO (100 ppm) (see Fig. 11).
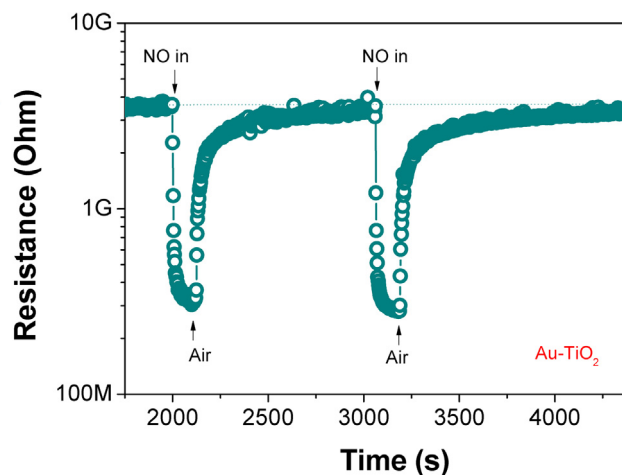
Comparing the response of all sensors in dark conditions (see Fig. 12a), it is clearly noted as the gold-promoted TiO$_2$ sensor shows a higher response with respect to pure and Ag-TiO$_2$, while for the Pt-TiO$_2$ sensor the response is much lower, following the ranking Au-TiO$_2$ > TiO$_2 \sim$ Ag-TiO$_2$ > Pt-TiO$_2$.

Based on these results, it appears that pure TiO$_2$ is intrinsically sensitive to NO at RT. The higher response obtained with the Au-TiO$_2$ sensor suggests that Au NPs act as an effective promoter for TiO$_2$ towards NO sensing, unlikely Ag and Pt. This latter behavior is linked to many factors, such as the nature of dopant, its concentra-
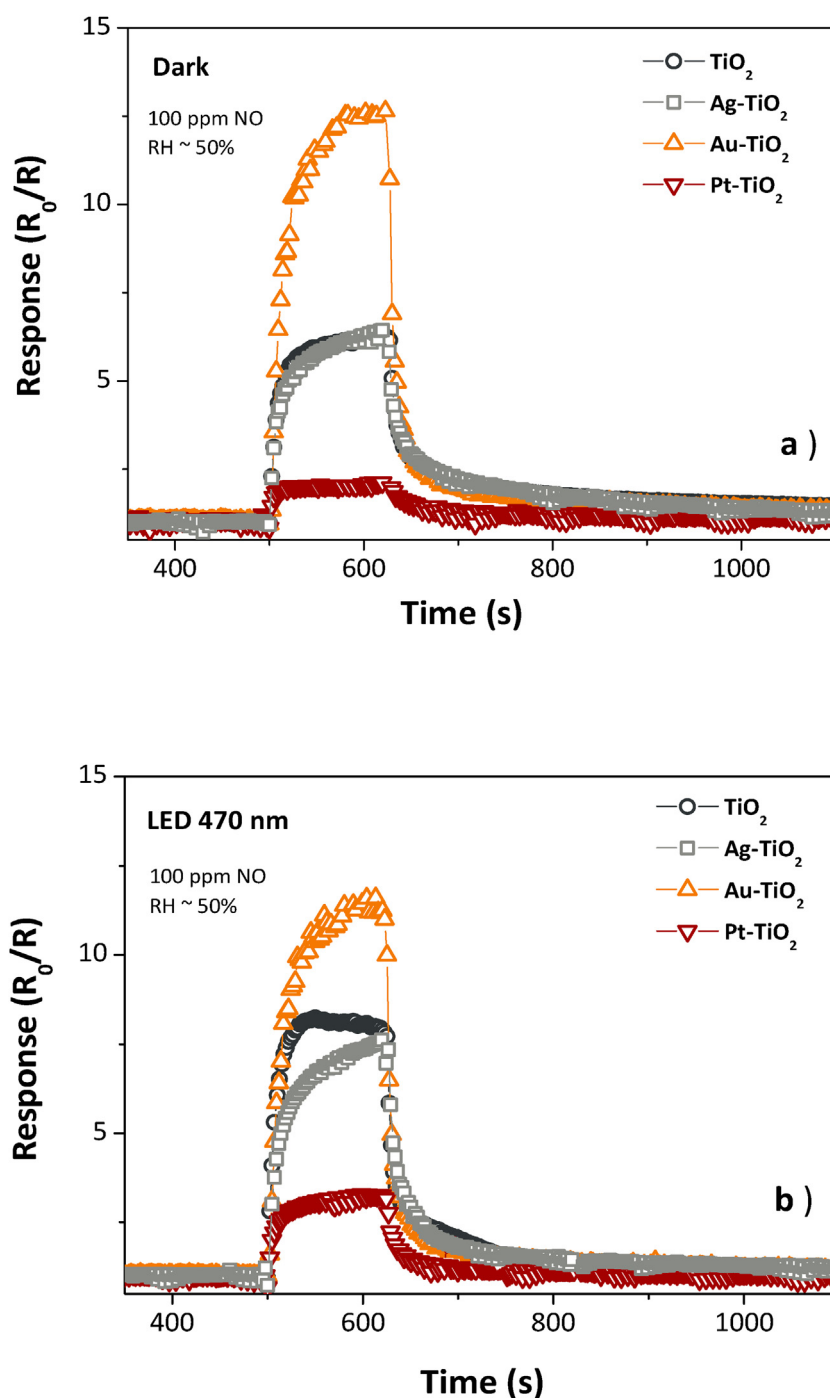
Fig. 12. Response of the investigated sensors towards 100 ppm of NO at room temperature under: a) dark and b) UV light (470 nm) conditions.

tion, oxidation state, shape and size of the metallic particles. This interesting aspect is planned to be investigated in a future work. It is well known that also UV irradiation can affect NO detection in metal oxide semiconductors [68], and this can occurs in different ways, i.e. enhancing the carrier generation, the density of free electron-hole couples and/or causing the photo-dissociation of the target gas.

TiO_2 and NM modifeid-TiO_2 nanostructures were then tested under various UV–vis light. Two LED having different wavelength, i.e. 400 and 470 nm, were used. Even if LED lamps used are not monochromatic, the window of emitted wavelengths is sufficiently narrow. During the entire period of the gas sensing measurement, the sensor surface was continuously irradiated. Results obtained

with LED at 470 nm, are shown in Fig. 12b. We can observe as the Au-TiO_2 sensor is still the most sensitive. However, this visible light appears to have almost no influence on the response of this sensor, providing instead the higher influence for the Pt-TiO_2 one.

To compare the results obtained, the efficiency of the LED irradiation on the sensor response, expressed by the relation: LED_{light} efficiency = R_{LED}/R_{DARK}, where R_{LED} and R_{DARK} represents the response under LED illumination and dark conditions, respectively, was reported for all sensors at the two wavelengths selected (Fig. 13). At 400 nm, pure TiO_2 displays the higher LED_{light} efficiency, which agrees with its higher absorbance at this wavelength (see Fig. 8) with respect the metal-doped TiO_2 ones. Vice-versa, at 470 nm, the Pt-doped sensor shows the higher LED_{light} efficiency,
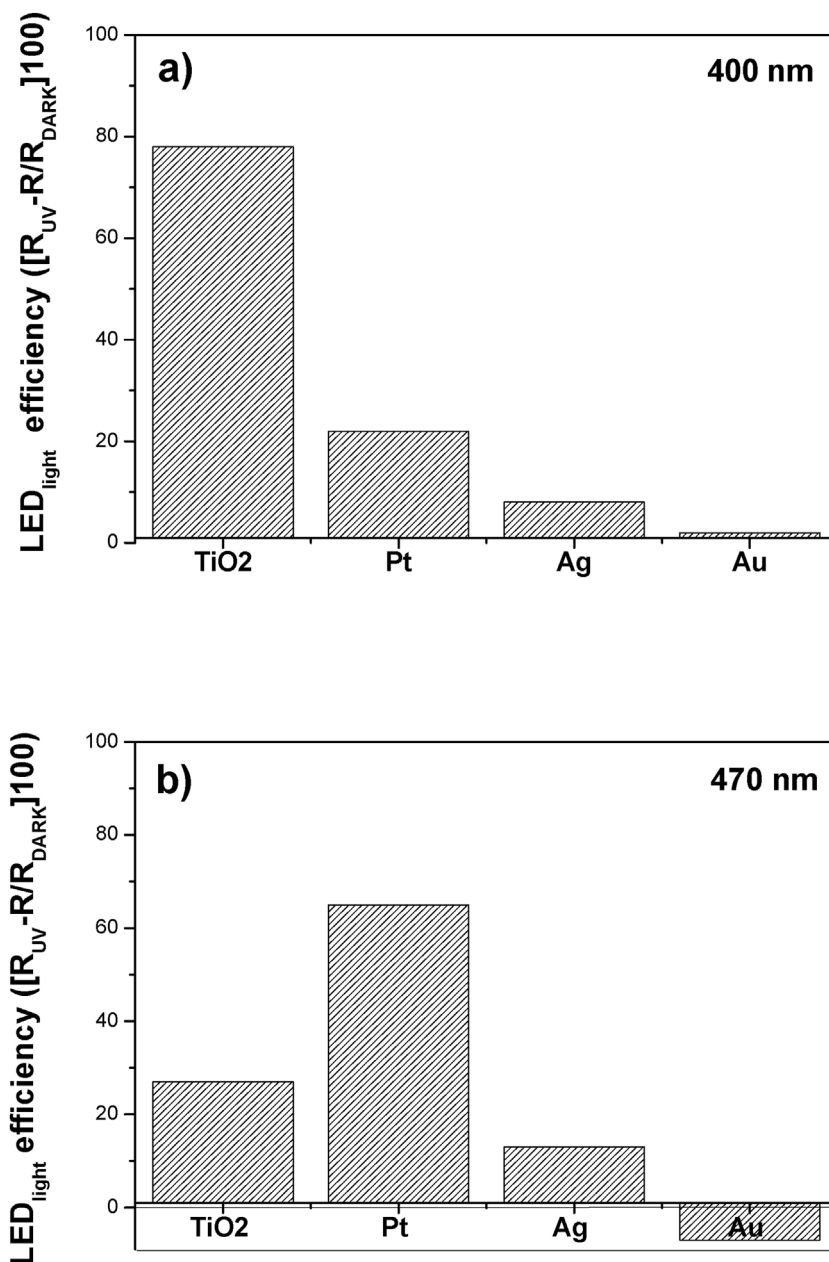
Fig. 13. LED$_{light}$ efficiency of the investigated sensors towards 100 ppm of NO at room temperature under LED light conditions at: a) 400 nm and b) 470 nm.

likely due to the strong plasmonic peak having the maximum around 500 nm.

This behavior can be explained examining the linear relationships reported in Fig. 14 between the LED$_{light}$ efficiency and the intensity of the adsorbed light, derived by the absorbance values at the selected wavelengths.

On this basis, we should expect that Au-TiO$_2$ may provide higher light efficiency working with a LED at around 600 nm, so enhancing more strongly its response to NO compared to that reported here with LED here used.

5. Conclusion

In summary, we have successfully obtained a new non-aqueous sol-gel process based on a low-temperature synthesis route for monodisperse titanium metal oxide nanoparticles. This new strategy was established to synthesize undoped and gold, platinum and silver metal decorated quasi/spherical TiO$_2$ nanoparticles, by using an original single metal oxide precursor, in one-pot-one-step procedure. The titanium(IV) oxyacetylacetonate TiO[CH$_3$COCH=C(O-)CH$_3$]$_2$, used as precursor, was an original starting clue to synthesize TiO$_2$ metal oxide nanoparticles. Therefore, the reaction between titanium(IV) oxyacetylacetonate and 1-hexanol was shown to be a straightforward process, which resulted in the formation of highly crystalline titania metal oxide nanoparticles with a small size of only 4.5 nm. A mechanism formation of the TiO$_2$ metal oxide nanoparticles was proposed and it was shown to proceed *via* a non-hydrolytic sol-gel route, involving ketone elimination.

Indeed, the introduction of small amount of metal nanoparticles either decorated/linked to surface of the titanium metal oxide nanoparticles supports not only the photocatalytic activity, but also
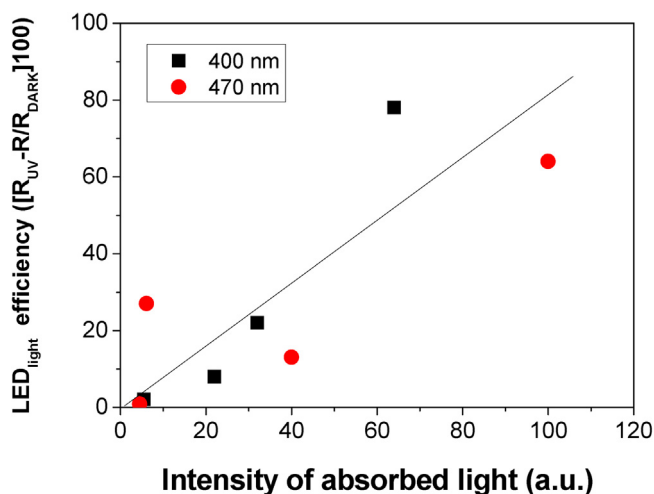
Fig. 14. LED$_{light}$ efficiency of the TiO$_2$ nanostructures as a function of the intensity of absorbed light at the selected wavelengths.

the gas sensing properties, thus giving a bifunctional material. The as-prepared gold doped TiO$_2$ NPs exhibited significantly enhanced NOx degradation, compared to the other NM@TiO$_2$ NPs.

Excellent results were also obtained with the same material (*i.e.* Au-TiO$_2$) using these nanostructures as sensing materials for the development of a conductometric NO sensor. A highly sensitivity sensor for NO determination based on Au-TiO$_2$ nanostructures and operating in both dark and under optimum LED light illumination was fabricated. Our results afford a new prospect for producing the multifunctional modified TiO$_2$ NPs for efficient gas sensing properties and photocatalytic activity.

Acknowledgements

Appendix A. Supplementary data

Supplementary data associated with this article can be found, in the online version, at 10.1016/j.apcatb.2017.06.010.

References

[1] W.L. Ong, M. Gao, G.W. Ho, Hybrid organic PVDF-inorganic M-rGO-TiO$_2$ (M = Ag, Pt) nanocomposites for multifunctional volatile organic compound sensing and photocatalytic degradation-H$_2$ production, Nanoscale 5 (2013) 11283–11290.

[2] D. Maspoch, D. Ruiz-Molina, J. Veciana, Old materials with new tricks: multifunctional open-framework materials, Chem. Soc. Rev. 36 (2007) 770–818.

[3] M. Karmaoui, E.V. Ramana, D.M. Tobaldi, L. Lajaunie, M.P. Graca, R. Arenal, M.P. Seabra, J.A. Labrincha, R.C. Pullar, High dielectric constant and capacitance in ultrasmall (2.5 nm) SrHfO3 perovskite nanoparticles produced in a low temperature non-aqueous sol-gel route, RSC Adv. 6 (2016) 51493–51502.

[4] M. Karmaoui, J.S. Amaral, L. Lajaunie, H. Puliyalil, D.M. Tobaldi, R.C. Pullar, J.A. Labrincha, R. Arenal, U. Cvelbar, Smallest bimetallic CoPt3 superparamagnetic nanoparticles, J. Phys. Chem. Lett. 7 (2016) 4039–4046.

[5] T.J. Wong, F.J. Lim, M. Gao, G.H. Lee, G.W. Ho, Photocatalytic H$_2$ production of composite one-dimensional TiO$_2$ nanostructures of different morphological structures and crystal phases with graphene, Catal. Sci. Technol. 3 (2013) 1086–1093.

[6] M.C. Ortega-Liebana, J.L. Hueso, R. Arenal, J. Santamaria, Titania-coated gold nanorods with expanded photocatalytic response. Enzyme-like glucose oxidation under near-infrared illumination, Nanoscale 9 (2017) 1787–1792.

[7] K.L. Kelly, E. Coronado, L.L. Zhao, G.C. Schatz, The optical properties of metal nanoparticles: the influence of size, shape, and dielectric environment, J. Phys. Chem. B 107 (2003) 668–677.

[8] K.A. Willets, R.P.V. Duyne, Localized surface plasmon resonance spectroscopy and sensing, Annu. Rev. Phys. Chem. 58 (2007) 267–297.

[9] R. Buonsanti, E. Carlino, C. Giannini, D. Altamura, L. De Marco, R. Giannuzzi, M. Manca, G. Gigli, P.D. Cozzoli, Hyperbranched anatase TiO2 nanocrystals: nonaqueous synthesis, growth mechanism, and exploitation in dye-sensitized solar cells, J. Am. Chem. Soc. 133 (2011) 19216–19239.

[10] M. Niederberger, M.H. Bartl, G.D. Stucky, Benzyl alcohol and titanium tetrachloride-A versatile reaction system for the nonaqueous and low-temperature preparation of crystalline and luminescent titania nanoparticles, Chem. Mater. 14 (2002) 4364–4370.

[11] M. Karmaoui, D.M. Tobaldi, S. Andrijana Sever, R.C. Pullar, M.P. Seabra, J.A. Labrincha, V.S. Amaral, Non-aqueous sol-gel synthesis through a low-temperature solvothermal process of anatase showing visible-light photocatalytic activity, RSC Adv. 4 (2014) 46762–46770.

[12] Y. Liu, A. Tang, Q. Zhang, Y. Yin, Seed-mediated growth of anatase TiO2 nanocrystals with core–antenna structures for enhanced photocatalytic activity, J. Am. Chem. Soc. 137 (2015) 11327–11339.

[13] L. De Trizio, R. Buonsanti, A.M. Schimpf, A. Llordes, D.R. Gamelin, R. Simonutti, D.J. Milliron, Nb-doped colloidal TiO2 nanocrystals with tunable infrared absorption, Chem. Mater. 25 (2013) 3383–3390.

[14] S. Sakthivel, M.C. Hidalgo, D.W. Bahnemann, S.U. Geissen, V. Murugesan, A. Vogelpohl, A fine route to tune the photocatalytic activity of TiO2, Appl. Catal. B: Environ. 63 (2006) 31–40.

[15] D.M. Tobaldi, R.A.S. Ferreira, R.C. Pullar, M.P. Seabra, L.D. Carlos, J.A. Labrincha, Nano-titania doped with europium and neodymium showing simultaneous photoluminescent and photocatalytic behaviour, J. Mater. Chem. C 3 (2015) 4970–4986.

[16] T. Sugimoto, X. Zhou, A. Muramatsu, Synthesis of uniform anatase TiO2 nanoparticles by gel–sol method: 1. Solution chemistry of Ti(OH)n(4-n)+ complexes, J. Colloid Interface Sci. 252 (2002) 339–346.

[17] D.M. Tobaldi, C. Piccirillo, R.C. Pullar, A.F. Gualtieri, M.P. Seabra, P.M.L. Castro, J.A. Labrincha, Silver-modified nano-titania as an antibacterial agent and photocatalyst, J. Phys. Chem. C 118 (2014) 4751–4766.

[18] M. Kitano, M. Matsuoka, M. Ueshima, M. Anpo, Recent developments in titanium oxide-based photocatalysts, Appl. Catal. A: Gen. 325 (2007) 1–14.

[19] G. Neri, First fifty years of chemoresistive gas sensors, Chemosensors 3 (2015) 1.

[20] J. Zhang, X. Liu, G. Neri, N. Pinna, Nanostructured materials for room-temperature gas sensors, Adv. Mater. 28 (2016) 795–831.

[21] M. Righettoni, A. Amann, S.E. Pratsinis, Breath analysis by nanostructured metal oxides as chemo-resistive gas sensors, Mater. Today 18 (2015) 163–171.

[22] K. Wetchakun, T. Samerjai, N. Tamaekong, C. Liewhiran, C. Siriwong, V. Kruefu, A. Wisitsoraat, A. Tuantranont, S. Phanichphant, Semiconducting metal oxides as sensors for environmentally hazardous gases, Sens. Actuators, B 160 (2011) 580–591.

[23] M. Penza, C. Martucci, G. Cassano, NOx gas sensing characteristics of WO3 thin films activated by noble metals (Pd, PtAu) layers, Sens. Actuators, B 50 (1998) 52–59.

[24] P. Scardi, M. Leoni, Whole powder pattern modelling, Acta Crystallogr. A 58 (2002) 190–200.

[25] M. Leoni, T. Confente, P. Scardi, PM2 K: a flexible program implementing whole powder pattern modelling, Z. Kristallogr. 23 (2006) 249–254.

[26] G. Caglioti, A. Paoletti, F.P. Ricci, On resolution and luminosity of a neutron diffraction spectrometer for single crystal analysis, Nucl. Instrum. Methods 9 (1960) 195–198.

[27] F.L. Toma, G. Bertrand, D. Klein, C. Coddet, Photocatalytic removal of nitrogen oxides via titanium dioxide, Environ. Chem. Lett. 2 (2004) 117–121.

[28] H. Zhang, J.F. Banfield, Thermodynamic analysis of phase stability of nanocrystalline titania, J. Mater. Chem. 8 (1998) 2073–2076.

[29] B. Puértolas, Á. Mayoral, R. Arenal, B. Solsona, A. Moragues, S. Murcia-Mascaros, P. Amorós, A.B. Hungría, S.H. Taylor, T. García, High-temperature stable gold nanoparticle catalysts for application under severe conditions: the role of TiO2 nanodomains in structure and activity, ACS Catal. 5 (2015) 1078–1086.

[30] E. Dehouck, A. Gaudin, N. Mangold, L. Lajaunie, A. Dauzères, O. Grauby, E. Le Menn, Weathering of olivine under CO2 atmosphere: a martian perspective, Geochim. Cosmochim. Acta 135 (2014) 170–189.

[31] C.B. Carter, D.B. Williams, Transmission electron microscopy, Springer-Verlag, US, 2009.

[32] C. Langlois, P. Benzo, R. Arenal, M. Benoit, J. Nicolai, N. Combe, A. Ponchet, M.J. Casanove, Fully Crystalline Faceted Fe–Au Core–Shell Nanoparticles, Nano Lett. 15 (2015) 5075–5080.

[33] M.G.I.N. Murdoch, M.A. Waterhouse, J.B. Nadeem, M.A. Metson, R.F.J. Keane Howe Llorca, H. Idriss, The effect of gold loading and particle size on photocatalytic hydrogen production from ethanol over Au/TiO2 nanoparticles, Nat. Chem. 3 (2011) 489–492.

[34] J.M. López, R. Arenal, B. Puértolas, Á. Mayoral, S.H. Taylor, B. Solsona, T. García, Au deposited on CeO2 prepared by a nanocasting route: a high activity catalyst for CO oxidation, J. Catal. 317 (2014) 167–175.

[35] M.P. Casaletto, A. Longo, A. Martorana, A. Prestianni, A.M. Venezia, XPS study of supported gold catalysts: the role of Au0 and Au + δ species as active sites, Surf. Interface Anal. 38 (2006) 215–218.

[36] J. Radnik, C. Mohr, P. Claus, On the origin of binding energy shifts of core levels of supported gold nanoparticles and dependence of pretreatment and material synthesis, Phys. Chem. Chem. Phys. 5 (2003) 172–177.

[37] P.S. Bagus, A. Wieckowski, H. Freund, The contribution of lattice strain to core-level binding energy shifts in metal nanoparticles: generality and origin of the shifts, Comp. Theor. Chem. 987 (2012) 22–24.

[38] C.D. Wanger, W.M. Riggs, L.E. Davis, J.F. Moulder, Handbook of x-ray photoelectron spectroscopy: a reference book of standard data for use in x-ray photoelectron spectroscopy, Physical Electronics Division, Perkin-Elmer Corp., Eden Prairie, Minn, 1979.

[39] S.W. Gaarenstroom, N. Winograd, Initial and final state effects in the ESCA spectra of cadmium and silver oxides, J. Chem. Phys. 67 (1977) 3500–3506.

[40] K. Hakouk, P. Deniard, L. Lajaunie, C. Guillot-Deudon, S. Harel, Z Wang, B. Huang, H.-J. Koo, M.-H. Whangbo, S. Jobic, R. Dessapt, Novel soft-chemistry route of Ag2Mo3O10·2H2O nanowires and in situ photogeneration of a Ag@Ag2Mo3O10·2H2O plasmonic heterostructure, Inorg. Chem. 52 (2013) 6440–6449.

[41] V.K. Kaushik, XPS core level spectra and Auger parameters for some silver compounds, J. Electron Spectrosc. Relat. Phenom. 56 (1991) 273–277.

[42] O. Frank, M. Zukalova, B. Laskova, J. Kurti, J. Koltai, L. Kavan, Raman spectra of titanium dioxide (anataserutile) with identified oxygen isotopes (16,17,18), Phys. Chem. Chem. Phys. 14 (2012) 14567–14572.

[43] F. Tian, Y. Zhang, J. Zhang, C. Pan, Raman spectroscopy: a new approach to measure the percentage of anatase TiO$_2$ exposed (001) facets, J. Phys. Chem. C 116 (2012) 7515–7519.

[44] F.C. Hawthorne, Spectroscopic methods in mineralogy and geology, Mineral. Soc. Am. 18 (1988).

[45] T. Luttrell, S. Halpegamage, J. Tao, A. Kramer, E. Sutter, M. Batzill, Why is anatase a better photocatalyst than rutile?—Model studies on epitaxial TiO2 films, Sci. Rep. 4 (2014) 4043.

[46] M. Prieto, R. Arenal, L. Henrard, L. Gomez, V. Sebastian, M. Arruebo, Morphological tunability of the plasmonic response: from hollow gold nanoparticles to gold nanorings, J. Phys. Chem. C 118 (2014) 28804–28811.

[47] R. Arenal, L. Henrard, L. Roiban, O. Ersen, J. Burgin, M. Treguer-Delapierre, Local plasmonic studies on individual core–shell gold–silver and pure gold nano-bipyramids, J. Phys. Chem. C 118 (2014) 25643–25650.

[48] R.G. Palgrave, I.P. Parkin, Aerosol assisted chemical vapor deposition using nanoparticle precursors: A route to nanocomposite thin films, J. Am. Chem. Soc. 128 (2006) 1587–1597.

[49] S. Eustis, M.A. El-Sayed, Why gold nanoparticles are more precious than pretty gold: noble metal surface plasmon resonance and its enhancement of the radiative and nonradiative properties of nanocrystals of different shapes, Chem. Soc. Rev. 35 (2006) 209–217.

[50] P.K. Jain, W. Qian, M.A. El-Sayed, Ultrafast electron relaxation dynamics in coupled metal nanoparticles in aggregates, J. Phys. Chem. B 110 (2006) 136–142.

[51] M.A. Martins, S. Fateixa, A.V. Girão, S.S. Pereira, T. Trindade, Shaping gold nanocomposites with tunable optical properties, Langmuir 26 (2010) 11407–11412.

[52] R.C. Pullar, S.J. Penn, X. Wang, I.M. Reaney, N.M. Alford, Dielectric loss caused by oxygen vacancies in titania ceramics, J. Eur. Ceram. Soc. 29 (2009) 419–424.

[53] P.N. Njoki, I.I.S. Lim, D. Mott, H.-Y. Park, B. Khan, S. Mishra, R. Sujakumar, J. Luo, C.-J. Zhong, Size correlation of optical and spectroscopic properties for gold nanoparticles, J. Phys. Chem. C 111 (2007) 14664–14669.

[54] J.Z. Bloh, A. Folli, D.E. Macphee, Photocatalytic NOx abatement: why the selectivity matters, RSC Adv. 4 (2014) 45726–45734.

[55] S.T. Kochuveedu, Y.H. Jang, D.H. Kim, A study on the mechanism for the interaction of light with noble metal-metal oxide semiconductor nanostructures for various photophysical applications, Chem. Soc. Rev. 42 (2013) 8467–8493.

[56] M. Jakob, H. Levanon, P.V. Kamat, Charge distribution between UV-irradiated TiO2 and gold nanoparticles: determination of shift in the fermi level, Nano Lett. 3 (2003) 353–358.

[57] V. Subramanian, E.E. Wolf, P.V. Kamat, Catalysis with TiO2/Gold nanocomposites. effect of metal particle size on the fermi level equilibration, J. Am. Chem. Soc. 126 (2004) 4943–4950.

[58] S. Linic, P. Christopher, D.B. Ingram, Plasmonic-metal nanostructures for efficient conversion of solar to chemical energy, Nat. Mater. 10 (2011) 911–921.

[59] Y. Tian, T. Tatsuma, Mechanisms and applications of plasmon-induced charge separation at TiO2 films loaded with gold nanoparticles, J. Am. Chem. Soc. 127 (2005) 7632–7637.

[60] A. Furube, L. Du, K. Hara, R. Katoh, M. Tachiya, Ultrafast plasmon-Induced electron transfer from gold nanodots into TiO2 nanoparticles, J. Am. Chem. Soc. 129 (2007) 14852–14853.

[61] D.O. Scanlon, C.W. Dunnill, J. Buckeridge, S.A. Shevlin, A.J. Logsdail, S.M. Woodley, C.R.A. Catlow, M.J. Powell, R.G. Palgrave, I.P. Parkin, G.W. Watson, T.W. Keal, P. Sherwood, A. Walsh, A.A. Sokol, Band alignment of rutile and anatase TiO2, Nat. Mater. 12 (2013) 798–801.

[62] H. Saito, Y. Nosaka, Mechanism of singlet oxygen generation in visible-light-induced photocatalysis of gold-nanoparticle-deposited titanium dioxide, J. Phys. Chem. C 118 (2014) 15656–15663.

[63] F. Dong, Z. Zhao, Y. Sun, Y. Zhang, S. Yan, Z. Wu, An advanced semimetal–organic Bi Spheres–g-C3N4 nanohybrid with SPR-enhanced visible-light photocatalytic performance for NO purification, Environ. Sci. Technol. 49 (2015) 12432–12440.

[64] Y. Hu, X. Song, S. Jiang, C. Wei, Enhanced photocatalytic activity of Pt-doped TiO2 for NOx oxidation both under UV and visible light irradiation: a synergistic effect of lattice Pt4+ and surface PtO, Chem. Eng. J. 274 (2015) 102–112.

[65] M.J. Hernández Rodríguez, E. Pulido Melián, D. García Santiago, O. González Díaz, J.A. Navío, J.M. Doña Rodríguez, NO photooxidation with TiO2 photocatalysts modified with gold and platinum, Appl. Catal. B: Environ. 205 (2017) 148–157.

[66] J. Yun, H.-I. Kim, Y.-S. Lee, A hybrid gas-sensing material based on porous carbon fibers and a TiO2 photocatalyst, J. Mater. Sci. 48 (2013) 8320–8328.

[67] L.-Y. Hong, H.-N. Lin, NO gas sensing at room temperature using single titanium oxide nanodot sensors created by atomic force microscopy nanolithography, Beilstein J. Nanotechnol. 7 (2016) 1044–1051.

[68] N.D. Chinh, N.D. Quang, H. Lee, T. Thi Hien, N.M. Hieu, D. Kim, C. Kim, D. Kim, NO gas sensing kinetics at room temperature under UV light irradiation of In(2)O(3) nanostructures, Sci. Rep. 6 (2016) 35066.